The Frontenac: An Autonomous Surface Vehicle

aQuatonomous at Queen's University

Omar Allam, Julian Tiqui, Logan Calder, Teema Mackay, Sarah Dube, Thomas Hung, Ethan Powell, Kate Aiken, Ethan Astri, Charles Debane, Lorenzo DeMarni, Jacob Badali

Abstract

aQuatonomous is a student-led interdisciplinary design team at Queen's University focused on the development of clean-powered Autonomous Surface Vehicles (ASVs) for ecological research and autonomous maritime robotics. This report presents the design philosophy, competition strategy, and system architecture of the 2025–2026 ASV, *The Frontenac*. The team prioritizes system reliability, modularity, and simplicity over excessive complexity to maximize consistent autonomous performance in the RoboNation RoboBoat competition. Design decisions across mechanical, electrical, autonomy, and systems integration domains are directly informed by competition task requirements and validated through simulation, laboratory testing, and open-water trials.

I. Competition Strategy

A. Adherence to Mechanical Constraints

The vessel, pictured in Fig. 1, is built to fit competition requirements while maximizing bridge space and load capacity to accommodate electrical components. The vessel features a catamaran design, measuring 3.55 ft in length, 3.02 ft in width and 1.92 ft tall. The hulls are 3D printed and wrapped with fibreglass to minimize weight while maintaining impermeability. The vessel has a mass of 45 lb, with a maximum load capacity of 150 lb and an optimal load of 45 lb. The ASV is designed to be modular for quick disassembly for transportation to the competition, with the bridge, electrical system, and individual hulls being detachable from one another. The wide beam of the catamaran increases transverse stability and reduces roll, providing a stable sensing and control platform during autonomous operation. The lightweight hull construction supports higher speeds and improved manoeuvrability under differential thrust control without compromising stability.

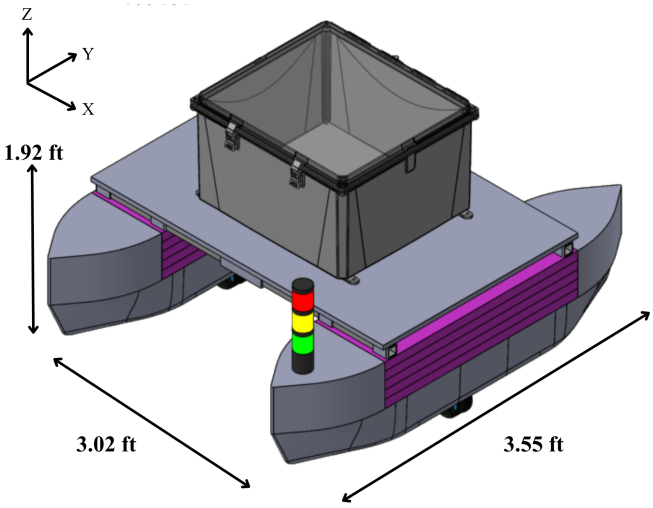

Figure 1: A complete CAD rendering of the ASV.

B. Sensor Selection

The ASV's sensing system is designed to reliably identify objects and objectives using a minimal number of strategically placed sensors, prioritizing simplicity. An M10 GPS and 6-Axis ICM-20689 IMU linked to a Pixhawk 4 Autopilot are used to localize the ASV in the global environment using an extended Kalman filter [1]. A secondary 9-Axis IMU is wired to a Jetson Orin Nano microcontroller for measurement redundancy, given the sensor noise present in the Pixhawk's onboard IMU.

A Unitree 4D LiDAR L1 is mounted at a 15-degree angle on the bow of the ASV for collision detection. The angle allows the LiDAR to detect obstacles that would have been below the plane of detection. In addition, LiDAR detections are cross-referenced with camera-based perception to verify object presence and range, improving robustness against false positives from either sensing modality.

Three Arducam 2.3MP AR0234 camera modules with a ~255-degree field of view are mounted on the bow of the ASV, with the port and starboard

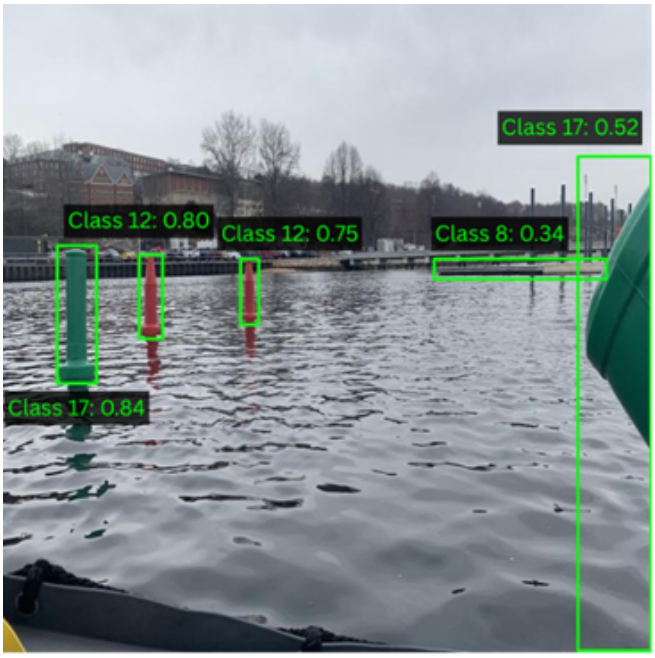

Figure 2: Example output from the YOLO-based camera detection pipeline. Detected competition elements are labelled with class identifiers and confidence scores before multi-camera fusion and LiDAR cross-referencing.

cameras angled outward toward the bow corners to maximize forward and lateral coverage. The side cameras allow for viewing signals and signage without having to maneuver the ASV, which is relevant for Tasks 3 and 5.

A compact USB microphone is integrated into the system to detect the acoustic burst required for the successful completion of Task 6.

C. Perception Base

1) Camera YOLO-Based Detection: A YOLO computer vision model was trained to detect all symbols, lights, and buoys present in the updated competition environment. Individual frames from the three onboard cameras are processed independently and fused into a unified X–Y–Z coordinate frame centred about the ASV. The YOLO model maps each detection from the camera image plane to distinct pixel-space coordinates, producing class labels and confidence scores, as shown in **Fig. 2**. The colour, size, and coordinate index of each detection are passed to an entity list, which is cross-referenced with LiDAR data to verify true object position relative to the vessel and reject spurious visual detections.

2) LiDAR Entity List Map: Mapped objects from LiDAR and camera detections are consolidated into a centralized entity list containing buoy height, distance, relative bearing, and visual attributes, including colour, presence of symbols, and presence/state of light. Each entity is positioned relative to the ASV in a shared reference frame and continuously updated by persistent tracking. This structured representation is consumed by the planning system to distinguish navigation buoys, obstacles, and task-specific markers, enabling task selection, collision avoidance, and waypoint generation. For example, when navigating between two buoys, the mapping system provides the global planner with the range and bearing of each buoy. If the left buoy is detected at a smaller bearing magnitude than the right buoy, the global planner determines that the vessel is offset from the desired centerline and generates a corrective waypoint to the right. This waypoint is passed to the local planner, which applies attractive forces toward the waypoint and repulsive forces from both buoys using the potential-field formulation.

D. Task Approach

The ASV uses a two-level planning architecture consisting of a task-aware global planner and a behaviour-tree-gated potential-field local planner. The global planner manages task sequencing, mission state transitions, and waypoint generation based on validated perception outputs. For Tasks 1 and 2, it generates waypoints centred between red and green gate buoys using their range and bearing, and advances mission state as gates are successfully transited.

The local planner executes these waypoints and applies obstacle avoidance using a potential-field formulation. Attractive forces pull the ASV toward the current waypoint, while repulsive forces are generated by nearby obstacles and buoys, scaled by their known attributes. Obstacle avoidance is activated only when required, when an object is in range of a threshold where a reverse manoeuvre is called, preventing interference with nominal tracking while ensuring collision-free motion through the

navigation channel and debris field.

In Task 3, the global planner identifies the entrance gate and, upon entry, classifies the colour indicator to determine the required turn direction. It then generates an apex waypoint on the appropriate side of the yellow buoy. The local planner manoeuvres by combining attraction to the apex waypoint with repulsion from the buoy and surrounding obstacles, before transitioning to exit gate waypoints to complete the task.

Task 4 was not selected for execution, as completing it would have required significant time and resources to design and integrate a dedicated delivery system for a single task, resulting in limited overall return relative to the effort involved.

In Task 5, cameras from the port and starboard sides detect unoccupied green slip docks and their corresponding numbers. Once all dock slips have been visited, an unoccupied slip with the lowest number is selected, and the boat returns to a waypoint outside that slip. LiDAR data is used to align the boat between the corners of the slip. The boat then moves forward while LiDAR provides real-time proximity data to planning, triggering motor shutdown at dock distance thresholds. Forward-facing coverage is sufficient as the vessel only approaches docks bow-first.

In Task 6, an onboard microphone detects the blast signal by analyzing continuous audio input in Fourier space. Once detected, it initiates an interrupt, causing the ASV to abandon its current task and seek a safe zone. The yellow buoys' locations are remembered by the ASV from the persistent tracking system. The ASV uses the local potential-field planner to avoid obstacles on its way to the yellow buoy.

A watchdog safety layer continuously monitors command activity and communication health. If manual control is not engaged within 120 s, or if no valid autonomous ROS command is received within 30 s, the ASV triggers a Return-to-Home (RTH) routine to recover the vessel in the event of signal loss or software failure.

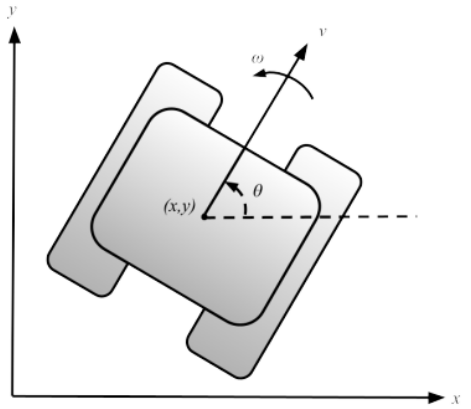

Figure 3: The control model of the ASV, where v represents thrust and ω represents steering (angular velocity). The vehicle state is represented by $[x, y, \theta]$.

II. Design Strategy

A. Mechanical Design

Hull Architecture and Construction: The vessel employs a twin-hull catamaran configuration to maximize stability and ensure predictable autonomous behaviour in wave-disturbed environments. This architecture was validated in the 2024 platform and is retained for the 2025 vessel to reduce mechanical risk and avoid re-validation of an unproven hull concept. The hull spacing is intentionally aggressive, resulting in a beam-to-length ratio of 1.18—significantly wider than conventional commercial catamarans (Fig. 1)—which prioritizes roll resistance and transverse stability. This near-square platform minimizes wave-induced disturbances, maintains stable sensor orientation, and enables consistent control performance under varying payload conditions [13]. Each hull is manufactured using a hybrid composite strategy consisting of a 3D-printed structural shell, internal foam core, and fibreglass outer skin, as illustrated in Fig. 1, enabling precise geometry control, reduced fabrication material, and passive flotation redundancy while maintaining competition-proven durability.

Propulsion and Control Strategy: The propulsion system uses differential thrust (tank steering), eliminating mechanical steering actuators and reducing moving components. This converts vehicle

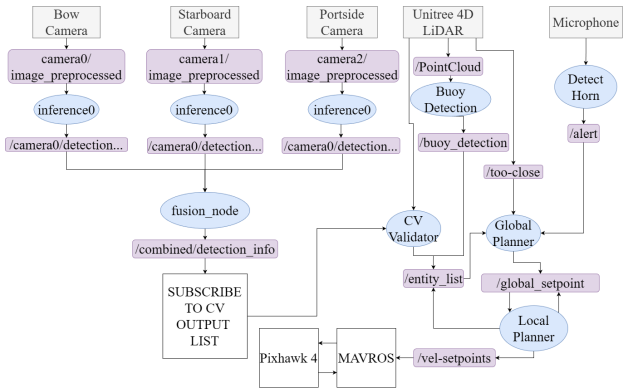

Figure 4: System-level autonomy architecture showing the computer vision, mapping, and planning pipelines and their ROS 2 interfaces.

control into a pure thrust-based problem, reducing control complexity while improving robustness and reliability during autonomous operation.

Scale, Payload Capacity, and Modularity: To address previous constraints on electrical expansion and iteration speed, the 2025 vessel increases hull volume and bridge area to decouple payload capacity from minimum operating mass. Increased buoyant reserve enables integration of additional computing hardware and sensor payloads without compromising freeboard or stability, prioritizing autonomy reliability over marginal mass reduction [14]. The mechanical structure is modular, with hulls, bridge, and payload systems designed as detachable subsystems.

B. Autonomy System

The autonomy system is built around an NVIDIA Jetson Orin Nano running ROS 2 Humble, selected for its GPU acceleration and low power consumption. LiDAR, cameras, and a microphone connect directly to the Jetson for perception and decision-making. A Pixhawk 4 autopilot interfaces with the Jetson via MAVLink over USB, offloading low-level control and enabling focus on high-level autonomy. The Pixhawk interfaces with GPS, IMU, compass, and the propulsion system, providing position, velocity, and attitude feedback to the Jetson. The autonomy stack generates high-level navigation commands, including desired positions and velocity vectors, which are executed by the Pixhawk through MAVROS. The system architecture is shown in Fig. 4. Propulsion is controlled by the Pixhawk using PWM signals to thruster ESCs and stepper motor drivers, with onboard PID control computing actuator commands. A rover-style frame is used, mapping one output channel to steering and one to thrust. Control signals are duplicated across both thrusters and stepper motors to simplify manoeuvring, as shown in Fig. 3.

Computer Vision: The vision system delivers real-time detections to autonomy via a ROS 2, TensorRT-accelerated multi-camera pipeline. Three parallel camera lanes (capture, preprocess, inference) publish into a combiner that outputs a fixed-rate, canonical `combined/detection_info` stream with stale-camera exclusion (Fig. 4). Inference runs a TensorRT FP16 `.engine`, with optional debug overlays. Images are captured at 1920×1200 @ 60 FPS and downsampled to 640×480; detections are reported as pixel-space bounding boxes [x1,y1,x2,y2]. On Jetson Orin Nano with YOLOv10m FP16, end-to-end latency is 30–45 ms (< 50 ms under load), sustaining 20–30 FPS per camera and a 30 Hz fused output. Resource usage is 45–65% GPU, 1.2–1.8 GB GPU memory, 20–35% CPU, and 1.5–2.5 GB system RAM. A single nine-class detector trained on ~21k images (70/20/10) is deployed via YOLO→ONNX→TensorRT and loaded once at startup with persistent GPU buffers (Fig. 2). The shared model supports all tasks, with lightweight downstream modules for colour indicators, supply-drop targeting, and docking number classification. Rule-based prefilters (ROI, size, and colour constraints) suppress irrelevant detections, improving stability without impacting real-time performance.

Mapping: The preprocessing pipeline applies spatial filtering to raw point clouds: horizontal range gating creates a configurable donut-shaped detection zone (0.5–50 m) excluding the vessel's hull and distant noise, while z-axis clipping removes overhead returns. Temporal buffering merges scans over a sliding 0.2 s window to increase point density for robust clustering. RANSAC plane fitting removes water-surface reflections before DBSCAN clustering. The density-based clustering operates in Carte-

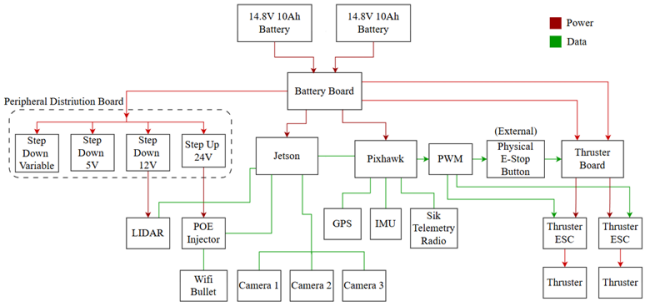

Figure 5: Electrical System Block Diagram.

sian (x, y) space with z-invariance to handle wave-induced vertical motion, preventing fragmentation of individual buoy detections. Cluster centroids are validated by geometric constraints (size, point count) and converted to polar coordinates (range, bearing) for navigation compatibility. Persistent tracking uses nearest-neighbour data association to maintain stable buoy identities across frames, with exponential smoothing of positions and persistence gating (e.g., $\geq$3 detections) to suppress false positives. Tracking continues through brief occlusions (e.g., $\leq$5 missed frames) before discard. Visualization markers are published to RViz. Tracked objects are checked for proximity and relative heading.

C. Electrical System

Electrical: The new design shown in Fig. 6 focuses on creating a modular system using smaller, more efficient components. Three printed circuit boards (PCBs) were created to handle power distribution, each containing fusing for short-circuit protection, power indicators, and live voltage monitoring where necessary. The Battery Board connects two 14.8 V LiPo batteries in parallel (rated to 70 A) and distributes power to the Jetson, Pixhawk, and complementary boards, while also including a full-system off switch for testing. The Peripheral Distribution Board contains three buck converters outputting 5 V, 12.8 V, and 24 V, as well as a variable converter for future expandability. The Thruster Board delivers power to both thrusters and contains emergency stop circuits. The ASV is designed to shut down upon pressing the physical E-stop button, receiving stop signals from the ground station, or if the connection between the boat and ground station is lost; a pull-down resistor provides a fail-safe shutdown if the E-stop wire is compromised. Gallium Nitride High Electron Mobility Transistors (GaN HEMT) were selected for the E-stop switching mechanism (see Appendix 4.6) over solid-state relays due to their high current capability, reduced power consumption, compact size, and switching speed. Thermal analysis identified the transistors as primary heat sources under full-load conditions (see Appendix 4.6), and heat sinks are used for dissipation. All current-carrying components and traces are rated for 120% of maximum current draw.

Telemetry: This year's design, shown in Fig. 6, ensures reliable developer-friendly interfacing and redundant connections if failure occurs. Primary communication uses a Ubiquiti NSM2 directional Wi-Fi bullet at the ground station paired with an AirMax M2 HP omnidirectional antenna on the ASV. The bullet antenna attenuates off-axis interference on the order of 10–15 dB [2]. For remote software development and computer vision verification, a data rate of 6- 8 Mbps is preferred [3]. A 915 MHz Wa66 LoRa telemetry connection is provided as a backup for terminal communications and control. Pixhawk communication is accomplished through SiK telemetry radio over Mission Planner, and RC is connected through an onboard receiver. To protect vital sensors from noise, aluminum Faraday caging is placed around high-current thruster lines to reduce H-field coupling [4].

III. Testing Strategy

A. Software Testing (Python/ROS2)

Planning behaviour was validated in ROS 2-based simulation using deliberate failure injection, including missing buoy detections, false obstacles, and GPS perturbations. Validation focused on behavioural outcomes, with success defined by collision-free operation and correct task execution.

B. Simulation Testing (Gazebo)

Gazebo is used to validate the interface between the autonomy stack and the ASV, confirming that high-level movement commands lead to expected motion

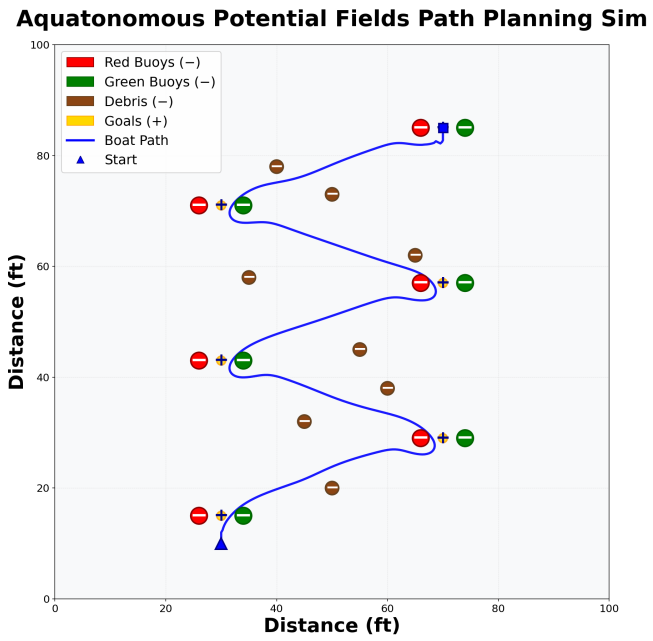

Figure 6: Potential Fields Simulation Graph.

in a repeatable environment. The tool supports open-loop motion testing and closed-loop autonomy validation. Controlled disturbances and fault cases such as command dropouts, latency, and thrust imbalance are occasionally introduced to test robustness.

C. Electrical Testing

To verify power system operation, the team individually tests the thruster and E-stop circuits to analyze and collect data on typical behaviour. To model thruster behaviour and boat power consumption, an oscilloscope was used to observe thruster I–V behaviour (Fig. 8). E-stop switching operation was tested using all three trigger methods to ensure thrusters are turned off in all scenarios, and a full-load test was conducted with all peripherals powered and thrusters at full output to identify maximum current draw. Telemetry testing verifies reliable and redundant communications by testing the primary Ubiquiti NSM2 directional Wi-Fi bullet and onboard AirMax M2 HP omnidirectional antenna over expected competition distances (25–100 m) and antenna orientations to confirm stable connectivity and assess interference rejection [2]. Link-budget checks (received power, sensitivity margin, SINR) are computed to confirm support for the required 6- 8 Mbps development throughput before deployment. A 915 MHz Wa66 LoRa link is tested under the same conditions as a backup terminal/-control channel, while Pixhawk SiK telemetry is validated through Mission Planner and RC override through the onboard receiver.

D. Autonomous Experimentation in a Wave Basin

The team has access to a laboratory wave basin for testing. Subsystem testing begins with manual RC operation to verify thruster functionality. Next, waypoints are sent from ground control using SiK telemetry radios and SSH into the Jetson Orin Nano to validate PID control and the Pixhawk's ASV model. Before autonomous testing, the perception system is verified by SSH into the Jetson to confirm segmentation from the bow camera and LiDAR. Autonomous navigation is tested by monitoring buoy navigation nodes as the ASV navigates between buoys under varied starting positions, angles, and wave conditions. At each stage (manual, waypoint, and autonomous), all E-stop systems (remote actuator, Jetson-controlled, soft, and physical) are triggered to confirm proper operation.

Acknowledgements

Acknowledgment is given to the Stephen J.R. Smith Faculty of Engineering, Honeywell, Claigan Environmental, Amidyne Solutions Ltd., and the Alma Mater Society of Queen's University's Sustainability Commission for their generous financial contributions. The Engineering Society of Queen's University is recognized for providing design bay space and operational support. Gratitude is extended to Dr. Joshua Marshall and Ph.D. Candidate Thomas Sears from Ingenuity Labs for technical advice and paper review, as well as to Dr. Ryan Mulligan and the Beaty Water Research Center for access to the wave basin and water research guidance, as well as the previous co-captains for their foundational contributions and support.

References

[1] Pixhawk, "Pixhawk 4 flight controller," 2021. [Online]. Available: https://docs.px4.io/main/en/flight_controller/pixhawk4.html Accessed: Jan. 22, 2025.

[2] Ubiquiti Networks, "NanoStation M2 Datasheet," 2026.

[3] AT&T, "Adaptive Bitrate Video Streaming Best Practices," 2026.

[4] Mossé Institute, "Faraday Cages," 2026.

[5] Cisco Systems, "Wireless Mesh Network Design Considerations," Cisco Technical Documentation, 2018. [Online]. Available: https://www.cisco.com.

[6] T. S. Rappaport, *Wireless Communications: Principles and Practice*, 2nd ed. Upper Saddle River, NJ, USA: Prentice Hall, 2002.

[7] MathWorks, "Friis transmission equation (RSS_Friis)," MATLAB File Exchange. [Online]. Available: https://www.mathworks.com.

[8] M. Tomała, "Analysis of interference and noise in wireless communication systems," Ph.D. dissertation, Wrocław Univ. of Science and Technology, 2019.

[9] A. B. Jones, "Noise figure and receiver sensitivity," QSL.net, 2004. [Online]. Available: https://www.qsl.net.

[10] Swiss Geoscience Commission, "Earth magnetic field intensity," ETH Zürich, 2016.

[11] OpenStax, "Magnetic fields produced by currents: Ampère's law," *College Physics*, Rice University, 2016. [Online]. Available: https://phys.libretexts.org.

[12] Blue Robotics, "T200 Thruster for ROVs, AUVs, and marine robotics." [Online]. Available: https://bluerobotics.com/store/thrusters/t100-t200-thrusters/t200-thruster-r2-rp/.

[13] M. R. Islam, M. M. Rahman, and A. K. M. A. Hossain, "Comparative study of catamaran and monohull vessels for livestock transportation," *Journal of Engineering Science and Technology*, vol. 14, no. 4, pp. 2237–2252, Aug. 2019.

[14] A. K. M. S. Islam, M. S. Hossain, and M. A. Rahman, "Structural and hydrodynamic performance analysis of catamaran hull forms," *Results in Engineering*, vol. 7, Art. no. 100304, 2020.

Table 1: Cisco wireless mesh metrics.

Bit Rate [Mbps]	linkSNR
6	14
9	15
12	16
18	18
24	22
36	26
48	29
54	31

IV. Appendix

A. Long Range Calculations

Calculations were made to confirm that there is an adequate Signal to Interference plus Noise Ratio (SINR), and sensitivity margin in competition-like environments. SINR is a quantity used to evaluate the upper bounds of data rate based on the received power and the noise-plus- interference. Different data rates require different SINR. The team referenced Cisco wireless mesh metrics.
[5]

Separately, the sensitivity margin is a ratio of the received power to the sensitivity of the device; this ensures that the radio can securely interpret the signal power it receives. Power received was determined at 100m and 200m, subtracting the output power by the free space power loss at that respective distance. The formula for free space loss (, in dB is given by [6]

$$\mathrm{FSPL}(d) = 32.45 + 20\log(f_{\mathrm{MHz}}) + 20\log(d_{\mathrm{km}}) \tag{1}$$

Received power is calculated with Transmitted from the ASV to the ground station. This has the highest data transmission requirements due to video transmission. This has a formula [7]

$$P_{\mathrm{rec}}[\mathrm{dBm}] = P_{\mathrm{Tx}}[\mathrm{dBm}] + G_{\mathrm{Tx}}[\mathrm{dBi}] + G_{\mathrm{Tx}}[\mathrm{dBi}] - \mathrm{FSPL}(d)[\mathrm{dB}] \tag{2}$$

Sensitivity margin is then determined by subtracting the receiver sensitivity from the received power. This margin is $\geq$ 30dB at the maximum data rate at 200m, which is far longer than any competitor's distance, which means power reception will not be a concern for the ASV.
SINR is the ratio of received power to noise plus interference. This is a measure of the received power relative to all other external noise. That

$$\mathrm{SINR} = \frac{P_{\mathrm{rec}}}{P_{\mathrm{noise}} + P_{\mathrm{interference}}} \tag{3}$$

$$\mathrm{SINR} = P_{\mathrm{rec}}[\mathrm{dBm}] - 10\log(P_{\mathrm{noise}} + P_{\mathrm{interference}}) \tag{4}$$

[8]
The noise power is determined by the noise floor, a constant of 6dB, plus the log of the bandwidth, minus thermal noise 174dBm.

$$P_{\mathrm{noise}}[\mathrm{dBm}] = 6[\mathrm{dBm}] + 10\log(B) - 174[\mathrm{dBm}] \tag{5}$$

[9]
No teams on competing channels
The interference is determined assuming that the other team's ASV will be at twice the distance from the ASV. If channels are distinct, then the effect of Interference is minimized due to adjacent channel rejection, and the effects of noise are only included. These create large margins of SINR that ensure a high data rate at each frequency. Directionality of the Wi-Fi bullet creates 10–15dB rejection of signals outside of radius [NSM2 datasheet]. When similar channel interference is included, the margin becomes approximately 20dB for 100m. This is safe for the goal connection speed, but could encounter issues, making switching channels preferable if nearby teams conflict. This shows that a bit rate in the range of 10Mbps could be supported, but also the importance of switching channels to switch to a mostly interference-free setup.

B. Wi-Fi Bullet testing data

At 0.5m transmitting from the unidirectional Wi-Fi bullet to the receiver of the NSM2 bullet, data transmission speeds were tested. Below are the results.
This was tested at a range of 5m, 50m, 100m, 150m, and 200m for the data rate connection, near Queen's

Table 2: Received power calculations for AirMax M2 Bullet to NSM2 Bullet.

	Transmitter (AirMax M2 Bullet)		Receiver (NSM2 Bullet)		Received power [dBm]	
Strength (Mbps)	Avg Tx [dBm]	Antenna gain [dBi]	Rx Sensitivity [dBm]	Antenna gain [dBi]	0.1 km	0.2 km
6–24 (11b/g)	28	9	-94	10.8	-32.37711058	-38.3977105
36 (11b/g)	25	9	-80	10.8	-35.37711058	-41.3977105

Table 3: Sensitivity margin at 0.2 km.

Strength (Mbps)	0.2 km [dBm]
6–24 (11b/g)	55.6022895
36 (11b/g)	38.6022895

supercomputing lab, with a difficult line of sight. These results show a higher interference and obstacles than at the comp. These are conservative expectations; further testing will be taken to best re-create competition situations. These still show over 10Mbits/sec at all expected lengths 100–150m.

C. Thruster Data

Thrust testing was performed to determine their I-V curves and compare them to the vendor- provided characterization. As shown in Figure X below, current is determined by using an oscilloscope to measure the voltage across a small shunt resistor using Ohm's law, current, I, equals voltage, V, over resistance, R.

$$I = \frac{V}{R} \tag{6}$$

The following waveforms were taken from the Oscilloscope at the following Pixhawk PWM 1900 [CSV_1], 1820 [CSV_2], 1700 [CSV_3]. The maximum, minimum, and average currents were recorded, as well as period and frequency for a single wave; these are recorded in the table below.
These data points are compared to the expected values, provided by the vendor, as validation. (Source 4)
This needs to be double-checked

D. Spectral Analysis

The properties of Faraday cages and their effectiveness are dependent on the frequencies of the corresponding H-fields. The thrusters take the largest

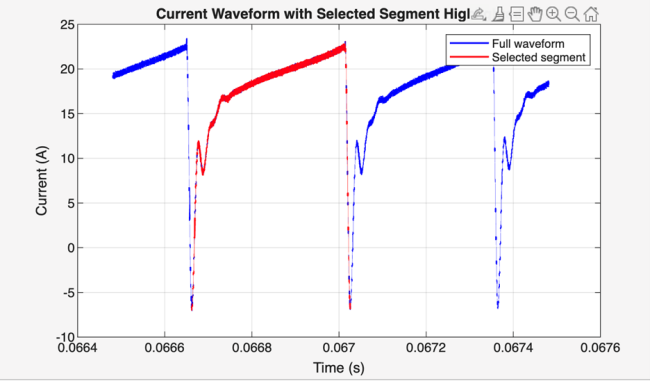

Figure 7: Current waveform with selected segment highlighted (PWM 1900).

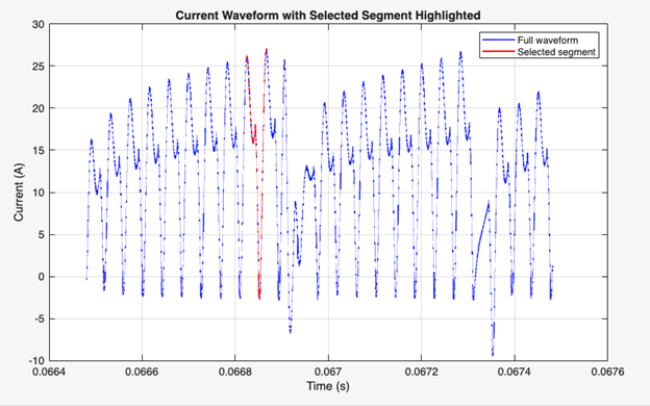

Figure 8: Current waveform with selected segment highlighted (PWM 1820).

current in the system by an order of magnitude and have dynamic fields. This led to spectral analysis of the signals to determine the frequency composition. The oscilloscope has a sampling period of $T_s = 500$ps or $F_s = 200$MHz. The magnitudes of current at are determined using DFT (Discrete Fourier Transform), $X[k]$ for the set of recorded points, $x[n]$. This has a frequency bin represented by integer k, over total points, integer N, where N is taken over one period to determine all the frequencies with spectral energy present in the signal.

Table 4: Sensitivity margin and minimum SINR margin at 0.2 km.

Strength (Mbps)	Sensitivity Margin (0.2 km)	Min SINR Margin (0.2 km)
6–24 (11b/g)	55.6022895	34.59
36 (11b/g)	38.6022895	27.59

Table 5: SINR with a team on the same channel.

Strength (Mbps)	SINR (Team on same channel)
6–24 (11b/g)	16.02050473

Table 6: Wi-Fi throughput at 0.5 m (time series).

Start [s]	End [s]	Bitrate [Mbps]
0	1	75.4
1	2	70.3
2	3	67.1
3	4	56.6
4	5	73.4
5	6	68.2
6	7	68.1
7	8	66.1
8	9	69.3
9	10	75.2
0–10 Average: 69		

$$|X[k]| = \frac{1}{N}\left|\sum_{n=0}^{N-1} x[n]e^{-j2\pi kn/N}\right| \tag{7}$$

Each frequency bin of the DFT is mapped to the CT (continuous time) frequency, f_k, with the following equation

$$f_k = \frac{kF_s}{N} \tag{8}$$

This leads to finding the current energy present at each frequency comprising the signal. Pixhawk PWM 1900, 1820, 1700.

E. Faraday Caging and Local Flux Closure

From the Fourier transformed thruster data shown in the thruster data analysis. The associated magnetic fields were analyzed to determine the fields at which the effect will be taken. From the earth's magnetic field of 25–65uT, IMU reference, magnetic fields

Table 7: Wi-Fi throughput versus distance.

Distance	Bitrate [Mbits/s]
5 m	20.765
50 m	14.5
100 m	13.82
150 m	11.08
200 m	0.577

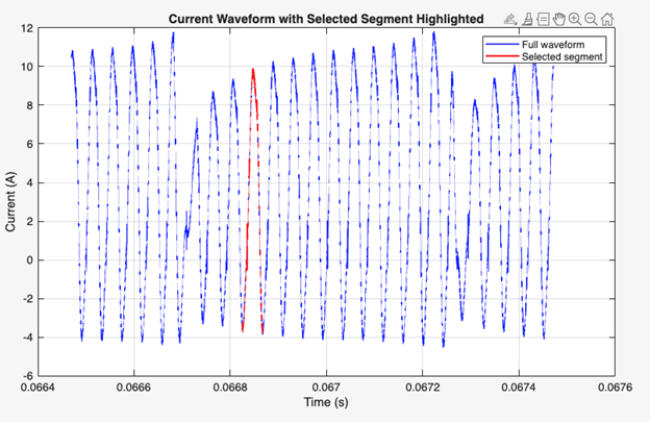

Figure 9: Current waveform with selected segment highlighted (PWM 1700).

greater than 25uT can have a serious effect on the integrity. [10]

From the thruster data, the associated magnetic field was calculated with the Biot-Savart Law [11]

for a long current-carrying wire; this was the simplest method since the exact geometry was not yet known. This is the magnetic field, B, times the permeability of free space, μ_0, $4\pi \cdot 10^{-7}$, since it is an air gap, multiplied by the current, divided by a constant and the shortest distance from the object to the wire.

$$B = \frac{\mu_0 I}{2\pi r} \tag{9}$$

But the distance was understood. This method leaves open that the geometry could increase the field by a factor of π. If in circular form, a factor

Table 8: Oscilloscope-derived current statistics at Pixhawk PWM commands.

ESC PWM (us)	Avg Current (A)	Max Curr (A)	Min Curr (A)	Period (s)	Frequency (Hz)
1900	17.5769	22.9583	-6.95833	363.3E-6	2.8E+3
1820	15.5656	27.0417	-9.4374	41.7E-6	24.0E+3
1700	3.6049	11.8125	-4.5	41.9E-6	23.9E+3

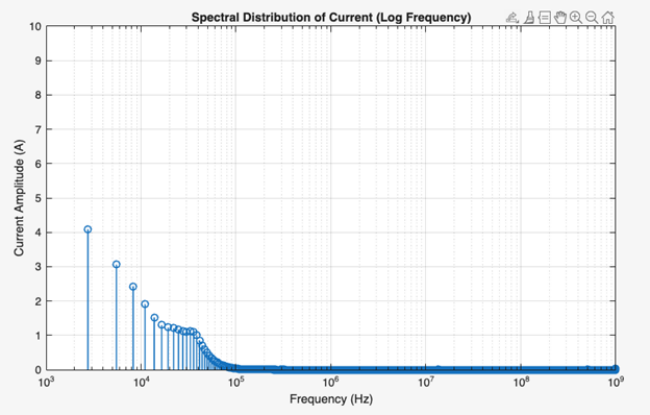

Figure 10: Spectral distribution of current (log frequency), PWM 1900.

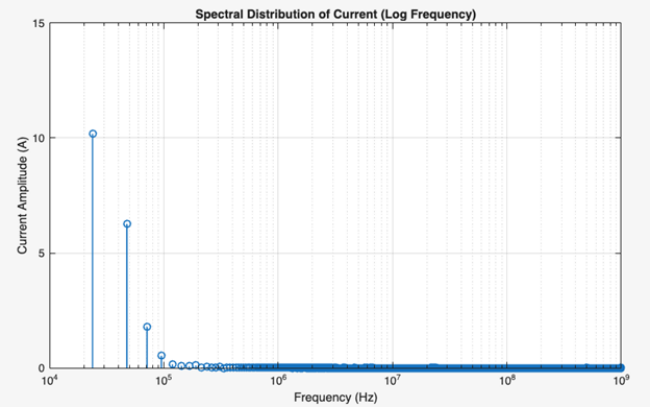

Figure 11: Spectral distribution of current (log frequency), PWM 1820.

of safety of 3.14 was the target. Analysis showed that a middle applied PWM of 1820, 23.81kHz could present problematic magnetic fields to the IMU within the 3.14 factor of safety. To reduce the effect of the fields, a cage of Aluminum material is used to dissipate the field as it leaves the thruster lines. This conductive material causes the magnetic field to dissipate. Ferrites are then added to reduce static fields since they are surrounding a point at a low frequency, not a travelling wave.
Original design for an aluminum Faraday Cage

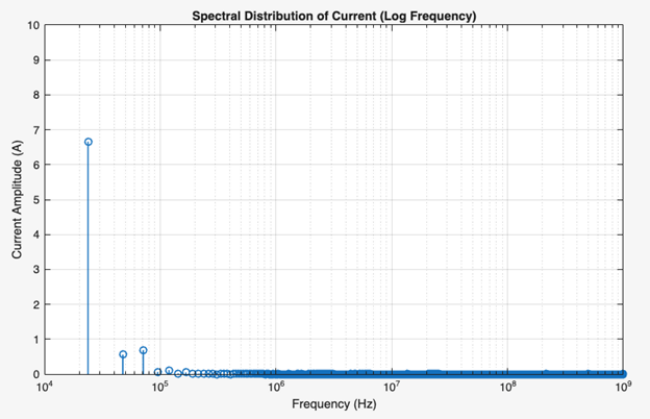

Figure 12: Spectral distribution of current (log frequency), PWM 1700.

F. E-stop Design

The new emergency stop system uses IGC025S08S1 Gallium Nitride High Electron Mobility. Transistors (GaN HEMT). These power transistors are rated for 80V, up to 86A, and measure 5mm x 3mm (reference 1). A gate driver is required for this transistor as it is more sensitive than a typical MOSFET. The 1EDN71x6U EiceDRIVER was chosen as it can provide the necessary current to switch the transistor safely and provides numerous internal safety features. The Pixhawk can only provide ~15mA, which will take much longer to switch the transistor, causing a large resistance that will generate significant heat that could damage the component. Its internal safety features include an active Miller clamp, which keeps the transistor off during voltage spikes, differential inputs, which ignore noise and allow us to “float” the voltage, and undervoltage lockout, which only turns on the transistor once the minimum threshold is reached (reference 2).
A gate to source voltage (V_{gs}) of 5V is needed to turn on this transistor. Since the transistor sits on the high side of our battery voltage, the gate must see 5V above battery voltage. Battery voltage can range

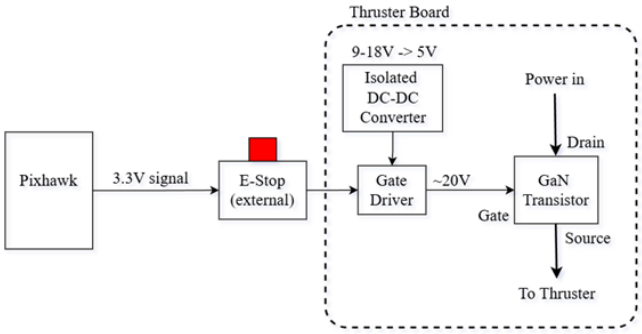

Figure 13: Block Diagram of E-stop circuit.

Component	# of Components	Current Draw (A)	Voltage (V)	Power (W)
Telem: Jetson + Pixhawk	1	7	14.8	103.6
Wi-Fi Bullet	1	0.29	24	6.96
4D Lidar	1	0.5	12	6
T200 Thruster	2	24	16	768
Max Output at Max Input	-	**55.79**	-	**884.56**
Avg. Output at Max Input		**41.79**		**660.56**
Battery Life (hrs) @ Theoretical Max		0.33 (19.8 minutes)		
Battery Life (hrs) @ Avg Max		0.56 (33.6 minutes)		

Figure 14: Figure of the Table of Power Consumption and Battery Life.

from 16V to 12V if overcharged or undercharged. To achieve a static 5V above battery voltage, a 9–18V variable input 5V output isolated DC-DC converter was used so that a “floating” ground at 14.8V could be employed. Both the converter and gate driver V- terminals are “floated” to the transistor source voltage of 14.8V, so that, despite a varying battery voltage, the gate driver will provide a static 5V above the battery voltage to operate the transistor.